Analysis of 3D kinetic simulations of meteor trails

Liane Tarnecki[1] **and Meers Oppenheim**[2]

[1]Aerospace Engineering Sciences, University of Colorado Boulder, Boulder CO, USA
[2]Center for Space Physics, Boston University, Boston MA, USA

Key Points:

- Neutral winds drive the development of waves along trails, particularly when the wind flows perpendicular to the trail and magnetic field.
- Spectra perpendicular to the magnetic field have acoustic-like behaviour moving close to the ion drift speed when a neutral wind is present.
- Waves tend to propagate perpendicular to the magnetic field, with power dropping off as a function of aspect angle.

Corresponding author: Liane Tarnecki, `liane.tarnecki@colorado.edu`

Abstract

Radars detect plasma trails created by the billions of small meteors that impact the Earth's atmosphere daily, returning data used to infer characteristics of the meteoroid population and upper atmosphere. Researchers use models to investigate the dynamic evolution of the trails, enabling them to better interpret radar results. This paper presents a fully kinetic, 3D code to explore the impacts of three trail characteristics: length, neutral wind speed, and ablation altitude. The simulations characterize the turbulence that develops as the trail evolves and these are compared to radar data. They also show that neutral winds drive the formation of waves and turbulence in trails, and that wave amplitudes increase with neutral wind speed. The finite trail simulations demonstrate that the bulk motion of the trail flows with the neutral wind. A detailed analysis of simulated trail spectra yield spectral widths, and evaluate signal strength as a function of aspect angle. Waves propagate primarily along the length of the trail in all cases, and most power is in modes perpendicular to $\vec{B}$. Persistent waves develop at wavelengths corresponding to the gradient scale length of the original trail. Our results show that the rate at which power drops with respect to aspect angle in meter-scale modes increases from 5.7 dB/degree to 6.9 dB/degree with a 15 km increase in altitude. The results will allow researchers to draw more detailed and accurate information from non-specular radar observations of meteors.

Plain Language Summary

As meteoroids travel through the atmosphere they leave behind trails of plasma. The Earth's geomagnetic field and atmospheric winds affect the behaviour of this plasma, changing the composition and properties of the local environment. We use large-scale computer simulations that track hundreds of millions of particles to model the evolution of meteor trails and the large electric fields they generate. This enables us to compare the effects of changing altitudes, winds, and trail shapes. The simulations show that winds in the neutral atmosphere drive the formation of waves that travel primarily along the length of the trail. We can also study the simulated meteors at multiple wavelengths and angles in order to obtain qualitative estimates of how radars would detect them. The conclusions drawn from these simulations can be tested by radar observations, and improve our understanding of the physics of meteor trails.

1 Introduction

The Earth's upper atmosphere is constantly bombarded by billions of much smaller meteoroids about the size of a grain of sand, moving at speeds greater than 20 km/s, most invisible to the naked eye. Between 75 and 110 km, meteoroid particles collide with neutrals, ionize, and ablate, leaving behind columns of plasma that can stretch tens to hundreds of meters. In the presence of Earth's geomagnetic field and electric fields that arise in the E-region ionosphere, these meteor trails develop turbulent waves as they diffuse and and cool. Large radars can measure the characteristics of theses trails. This paper presents 3D simulations of the plasma trails resulting from such meteoroids.

Meteors have significant impact on the atmosphere at large scales. Upon entering the atmosphere, meteoroids can impact and damage spacecraft. As meteoroids ablate, they deposit layers of metallic material measured by numerous optical instruments and used to track winds in the upper mesosphere and lower thermosphere. Meteor metals also modify the chemistry of this region and impact ionospheric densities and conductivities. Dust and particles left behind seed water clouds. Characterizing and understanding meteors can help researchers mitigate risk to spacecraft and help them observe and model the upper atmosphere.

Meteor observations have been commonly used to study the dynamics of atmospheric winds and, more recently, temperatures. Radar can observe trails moving with the neutral wind, and use drift speed as a proxy for wind velocity (Hocking & Thayaparan, 1997). These observations are incorporated into large scale atmospheric models. In the last few years, researchers have begun to use meteor radar estimates to determine mesospheric temperatures (Lee et al., 2016; Liu et al., 2017; Wen et al., 2014).

The majority of meteor data are from radar observations. Large radar arrays like the Jicamarca Radio Observatory (JRO) detect hundreds to thousands of trails every hour (Oppenheim et al., 2008). A detailed description of meteor observations with radar can be found in Chau and Woodman (2004). Optical measurements are possible and provide a second method for estimating meteor parameters such as mass, but the small meteors studied here are difficult to detect optically (Michell et al., 2015). Rockets have provided valuable but sparse in situ data with a single detection of an enormous trail (Kelley et al., 1998).

Large radars detect two distinct signals arising from meteor plasmas. They first detect plasma as it initially forms around the meteoroid when it begins to ablate. This is called the head echo. High-power large-aperture (HPLA) radar readily observe these, sometimes many times per second, and are commonly used to determine properties of the meteoroid. Assuming the head echo moves approximately with the meteoroid, one can constrain the velocity, orbital parameters, and mass of the particle (Close et al., 2005). Milliseconds after an HPLA radar observes a head echo, they can often observe a non-specular echo. These echoes are caused by reflections off of waves in the column of plasma left behind by the ablating meteoroid (Dyrud et al., 2012).

The geometry of a meteor observation impacts the data. Specular echoes occur when the radar beam and the meteor trail are close to perpendicular. This configuration returns a strong signal, and can be observed by small aperture radar. Historically, meteor radar observed specular trails (Sugar, 1964). Non-specular echoes occur when the trail is approximately perpendicular to the background magnetic field but not the radar beam. They result from Bragg scattering off field-aligned irregularities in the plasma trail (Chapin & Kudeki, 1994). The simulations analyzed in this paper model all trails, but the wave structure primarily concerns non-specular trails.

Radar observations lend themselves to spectral analysis. Chapin and Kudeki (1994) shows the time evolution of the spectrum from a single meteor observed at JRO. They show that a low-Doppler shift peak persists as the trail evolves and develops high-Doppler shift modes. Many spectra develop asymmetric ”wings” of power at high Doppler shift that gradually disappear. Hall et al. (1997) gives spectral widths for thousands of trails observed by the SuperDARN network, along with wind and velocity measurements.

Close et al. (2008) used observations from ALTAIR to study the relationship between signal strength and the angle between the trail and the magnetic field (called the aspect angle). They found that signal strength falls off 3 to 4 dB per degree as the radar moves away from perpendicular to the magnetic field for ALTAIR’s 160 MHz beam. Close et al. (2008) also investigated signal strength as a function of wavelength. They found that for non-specular trails, signal strength was proportional to λ^6, with some altitudinal variation. This roughly agrees with the theoretical prediction in Eshleman (1955) for short wavelength trails.

Radar observations are limited in several ways. Many radar have spatially-fixed arrays and only observe in one direction. This limits the radar to observe at fixed angle with respect to the Earth’s magnetic field. Radar also observe only one wavelength, but meteor trails generate waves at a wide range of scales.

To complement observations, researchers use simulations to explore the 3D structure and multi-scale modes of meteor trails. Simulations allow researchers to study all angles and modes present in a trail. The goal of such simulations is to produce predictions that can be tested through observation, and to test physical assumptions about meteors and their environment. In conjunction with observations, simulation results can help researchers interpret results and improve our understanding of meteor evolution.

The first fully 3D simulations of meteor trails were published in Oppenheim and Dimant (2015). They simulated two trails perpendicular to a magnetic field, with and without an incident neutral wind. Oppenheim and Dimant (2015) found that strong ambipolar electric fields caused the formation of plasma ridges along the background magnetic field. The simulation with no neutral wind developed only low-amplitude waves, even at the longest timescales. The added wind led to the development of strong waves, with wavelengths that grew from short to long over the course of the simulation. Trails in simulations with a neutral wind $\vec{E} \times \vec{B}$ drifted with the background electric and magnetic fields. This paper builds on those simulations and introduces new analysis.

2 Simulation Methods

Simulations were conducted using EPPIC, the particle-in-cell (PIC) code developed in Oppenheim and Dimant (2004), Oppenheim and Dimant (2006), and Oppenheim and Dimant (2013), among others. This electrostatic PIC code is well suited to modeling this problem, as it capture all kinetic processes including particle heating and Landau damping of waves. EPPIC simulates fully kinetic, collisional plasmas using ion and electron macroparticles, and can include externally imposed electric and magnetic fields E_0 and B_0.

The simulated plasma consists of several billion ions and electrons (see Birdsall and Langdon (1985) for a full treatment of PIC methods). EPPIC allows collisions with neutrals, which have a uniform background density. All collisions in EPPIC are electron-neutral or ion-neutral, where the probability of a collision is proportional to the macroparticle's velocity. There are no Coulomb or neutral-neutral collisions. A more complete description of the collision mechanism can be found in Oppenheim and Dimant (2004).

Like all kinetic PIC codes, this method requires some adjustment of physical parameters for numerical efficiency. Notably, the electron mass is artificially inflated to 44 times the true value (Oppenheim & Dimant, 2013). Background parameters closely mimic those in Oppenheim and Dimant (2015) For computational efficiency, the background density has a lower value than one would likely find naturally. Oppenheim and Dimant extensively tested these adjustments to ensure that simulations using these more efficient parameters produce similar results to far more expensive runs using more physically accurate parameters. The simulations in this work were tested with multiple background densities, with only marginal differences in outcome. All simulations use the same parameters, except where noted. See Table 1 for a list of simulation parameters.

The simulations presented here use a more efficient field solver than Oppenheim and Dimant (2015). This rapid spectral technique requires periodic boundary conditions in all directions. Effectively, this means that the simulation box is surrounded by identical boxes. For a meteor simulation, this effect is physically equivalent to an infinite number of meteors laid out on a grid. The dimensions must be carefully chosen to avoid contact between the meteor and its 'neighbors'. Unfortunately, it is impossible to avoid contact in all directions, due to the mobility of electrons along magnetic field lines. The dimension along B is made as large as feasible given computational resources, but complete isolation of the trail is impossible.

The geometry of a trail is as follows. The trail extends along the $\vec{x}$ axis, and a magnetic field of $\vec{B} = 0.5$ G points along the $\vec{z}$ axis. The initial trail consists of a smooth, thermalized plasma column in a neutral background. The peak column density is 120 times the background neutral density of 100 cm^{-3}, and falls off as a Gaussian with a vari-

Table 1. Simulation parameters.

Parameter	**Value**
B_z	0.5 G
Number of Ions	2×10^{11}
Number of Electrons	1×10^{11}
Simulation electron mass	44m_e
Grid cell size	$0.05 \times 0.05 \times 0.05$ m
Box Size	$25.6 \times 25.6 \times 102.4$ m
Neutral temperature	300 K
Time step	1.25×10^{-6} s

ance of 0.8 m. As the computational cost of each simulation increases with plasma density, this density value was selected as a compromise between a more realistic, denser plasma and a simulation that would complete in a reasonable amount of time. The Gaussian column is a reasonable assumption for the shape of the thermalized plasma trail, but the veracity of this claim is investigated with models of meteoroid ablation and trail formation in other work(Sugar et al., 2018).

Simulations with a neutral wind apply an additional 5 mV/m electric field $\vec{E_0}$ directed along the trail ($\vec{x}$), to shift into the frame of the wind. This corresponds to a 100 m/s wind in the $-\hat{y}$ direction. Note that because the frame transformation used places the simulation in the frame of the neutral wind, the whole simulation box can be thought of as moving with the wind and any motion inside the box as in addition to this bulk motion.

Two trail-end geometries are tested. The trail either extends across the entire box, or falls off exponentially at the edges. These edge conditions respectively produce effectively infinitely long trails and short, finite segments. Further discussion on the physicality of these simulations appears in the following section.

In order to simulate meteors at different altitudes, the collision rates for ion-neutral and electron-neutral collisions are adjusted. In this case, both collision rates are reduced by one e-folding, corresponding to an increase in altitude of about a scale height. Our baseline run approximates conditions at 100 km, and a second, otherwise identical run, approximates collision rates found at 115 km. While only two altitudes are tested in this work, additional cases can be explored in future work.

3 Results

Oppenheim and Dimant (2015) presented the first 3D kinetic PIC simulations of meteor trails. In this paper, those simulations are improved and the impacts of varying three simulation parameters are explored: trail-end geometry, neutral wind speed, and altitude. The spectra perpendicular to and off of $\vec{B}$ of the simulated trails are examined in order to evaluate signal strength as a function of wavelength and field alignment.

The simulation box is 512 x 512 x 2048 grid cells, with a grid cell size of 0.05 meters in all directions. Thus, the entire box extends 25.6 x 25.6 x 102.4 meters. These simulations improve upon the resolution of those in Oppenheim and Dimant (2015) by a factor of two. Each simulation time step is 1.25 μs for 31200 steps, for a 39 ms total simulation. Each simulation runs for over 15 hours on 4096 processors using the Stampede 2 supercomputer.

3.1 Trail evolution

In all cases trails diffuse quickly at the beginning of the simulation. Most of this initial diffusion occurs along $\vec{B}$, due to the mobility of electrons along the magnetic field, and the same formation of plasma ridges noted in Oppenheim and Dimant (2015) is observed. Waves develop in all cases, though amplitudes are small in cases with no neutral wind. To the eye, the most prominent mode is $\lambda = 2{-}3$ m. Waves typically form with small amplitudes, then grow. Without a neutral wind, waves quickly reach a maximum amplitude, but with a wind the amplitude continues to grow for the duration of the simulation time. The physical extent of the waves can sometimes grow to the scale of the trail width, resulting in some fracturing of the main body of the trail.

Figure 1 shows the evolution of ion density in the plane perpendicular to $\vec{B}$ in a simulation with a 100 m/s neutral wind. The simulation resolution is 5 cm in all dimensions, reduced for output to 10 cm. In simulations with no neutral wind, waves form on both sides of the trail in the plane perpendicular to both the trail and $\vec{B}$ (the xy plane). They tend to propagate in the $\vec{x}$ direction on the top side of the trail, and in the $-\vec{x}$ direction on the bottom side. The introduction of a neutral wind breaks the symmetry and causes waves not to develop on the bottom side of the trail, and have larger amplitudes and more turbulence on the top side. For a neutral wind vector $\vec{u}$, turbulence tends to develop where $\vec{u} \parallel \nabla n$.

The simulations with a neutral wind tend to $\vec{E} \times \vec{B}$ drift in the $-\vec{y}$ direction. Real trails likely do not $\vec{E} \times \vec{B}$ drift, and stay instead with the neutral wind. This assumption is tested by modifying the trail-end geometry in Section 3.2. Note that, as real trails extend through regions in which neutral winds change dramatically, a single trail can be carried along at different speeds along its length.

These results explore only uniform wind fields at two neutral wind speeds. However, additional simulations have shown that the relationship between neutral wind speed and turbulence is as expected. Faster neutral winds drive stronger turbulence that develops faster, but do not appear to trigger significantly different phenomena.

3.2 Finite trail simulations

In Oppenheim and Dimant (2015), periodic boundary conditions create a trail of effectively infinite length. The trail extends along the entire simulation box, and particles and fields wrap from one side of the system to the other. This is a non-physical geometry, and can prevent the development of ambipolar electric fields within the trail. To test the impact of finite trail edges, several simulations in which the density of the trail falls off exponentially at the ends of the trail were run, creating a short segment of plasma. Due to computational constraints, the main body of these simulated trails is only 15 meters long, and density falls off over an additional 5 meters on each end. Meteors in nature are comparatively larger, and can reach up to tens of kilometers in length (Dimant et al., 2009; Sugar et al., 2018). However, the plasma density along real trails likely varies due to differential ablation or fracturing of the meteoroid. Periodic boundary conditions on these simulations also effectively create an array of short trail segments. A truly accurate simulation of real meteors lies somewhere between segmented and infinite trails presented here.

The finite trails show a few differences in evolution from the infinite simulations. In the these simulations, waves develop first near the ends of the trail, then propagate toward the center. Figure 2 shows that in simulations with incident neutral winds, the ends of the trail often deform and bend away from the rest of the trail. Notably, trails with finite edges follow the neutral wind, rather than $\vec{E_0} \times \vec{B}$ drifting as infinite trails do. Particles moving along $\vec{E_0}$ build up at the edges of the trail, leading to a build up of charge that introduces a polarization electric field $\vec{E_{pol}}$ directed anti-parallel to $\vec{E_0}$.

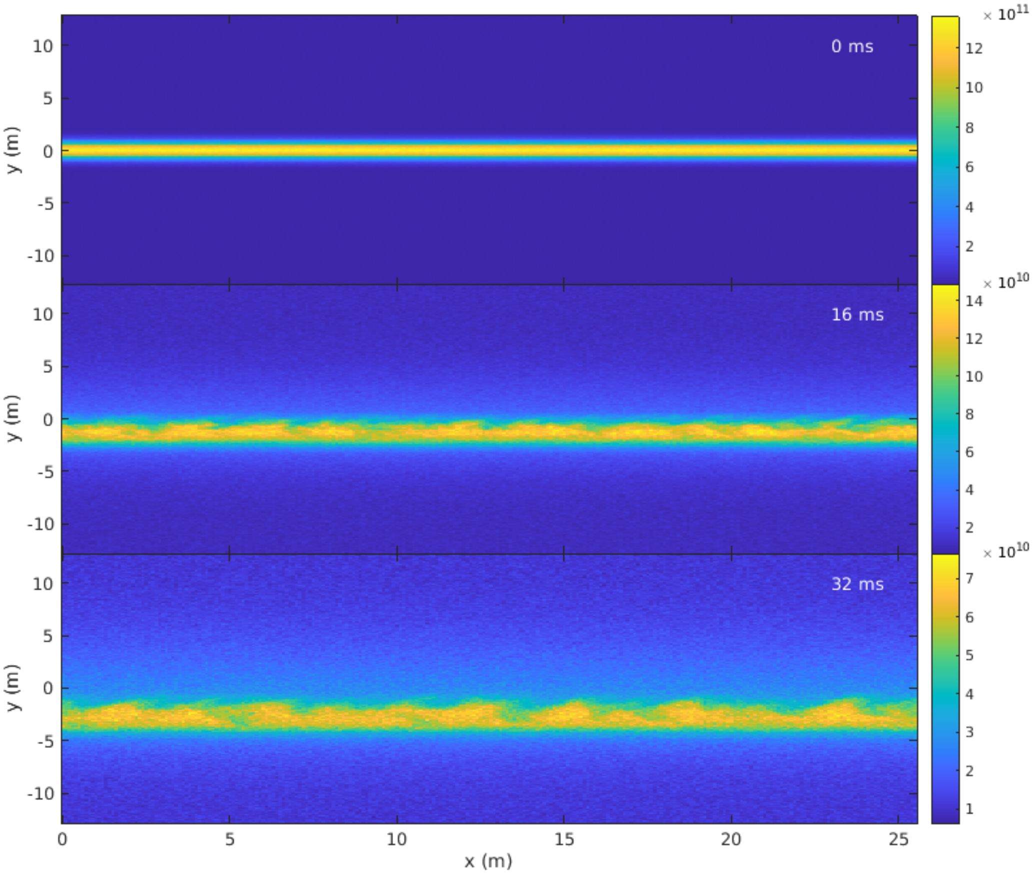

Figure 1. Ion density evolution of an infinite-trail simulation at 100 km with an incident neutral wind of 100 m/s. Cuts are through the center of the trail in the xy-plane, and $\vec{B}$ points out of the page. Density is in m^{-3}. Video included in supplementary information.

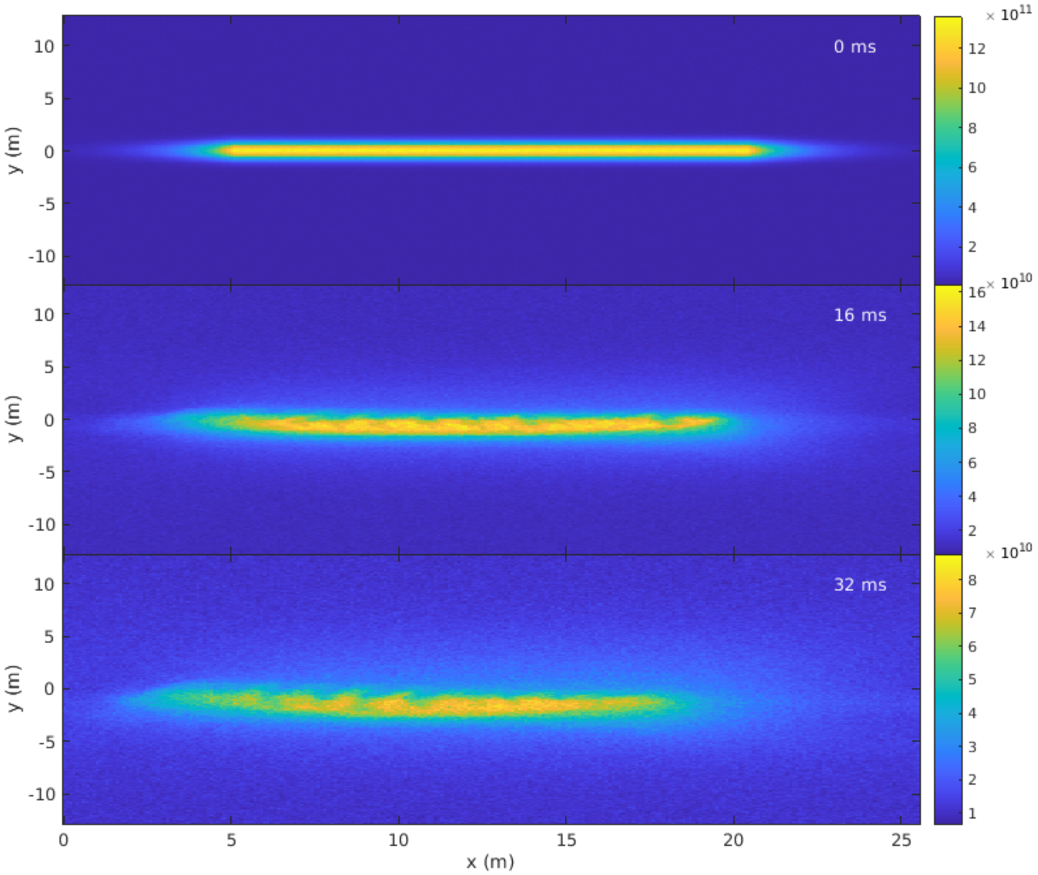

Figure 2. Ion density evolution of a finite-trail simulation at 100 km with an incident neutral wind of 100 m/s. Cuts are in the plane perpendicular to $\vec{B}$ and through the center of the trail. Note that the ends of the trail are deformed as the simulation progresses, and the trail as a whole drifts in the direction of the neutral wind. Video included in supplementary information.

$\vec{E_{pol}} \times \vec{B}$ pulls the trail in the positive $\hat{y}$ direction and works against the $\vec{E_0} \times \vec{B}$ drift. Importantly, the trail then generally moves only with the neutral wind. This is in contrast to the behavior of the infinite trails, and is in agreement with the theory discussed previously. Waves also develop slightly sooner in finite trail simulations. However, these changes have little impact on the evolution and behavior of the trails as a whole. Once waves have developed fully finite and infinite trails behave similarly, and spectra from finite trails do not differ significantly from those of infinitely long trails.

These results indicate that infinite trails capture the same general behavior and physics as the finite trails, with the exception of the $\vec{E} \times \vec{B}$ drift noted above. The finite trail simulations deserve further consideration, especially as computers improve and larger physical scales can be achieved, but at this time they provide little additional insight. As the finite trail segments are more likely to introduce numerical complications to the simulation (due to communication between ”neighboring” segments), all further discussion in this paper concerns only infinite simulations, unless otherwise noted.

3.3 Spectral analysis

The 3D simulations allow the extraction of measurable spectral quantities comparable to radar observations. The meteor trail power spectra as a function of frequency and wavenumber and the rate of power decay as a function of angle off of $\perp \vec{B}$ are explored.

3.3.1 Spectra perpendicular to $\vec{B}$

Power spectra are useful indicators of the types of wave modes that develop in the simulation. Because 4D spectra (k_x, k_y, k_z, ω) can be difficult to work with, slices of spectral space are selected. The mobility of electrons along the magnetic field works to short out the formation of waves in this direction, so the spectra perpendicular to $\perp \ \vec{B}$ are particularly emphasized.

Figure 3 shows the evolution of the spectrum perpendicular to $\vec{B}$ for the simulation with a wind. The spectra show four stages. At t=0, the spectrum of the body of the trail appears as a sharp peak at $k_x = 0$. This peak persists throughout the simulation, though it drops in amplitude and broadens through the run as the trail diffuses. To better display the spectra of the developing waves, the maximum power displayed in Figure 3 is capped at 85 dB. Turbulence first develops with peak power around $k_x = 5 \text{ m}^{-1}$, corresponding to 1.3 m wavelengths. As the simulation continues, the peak spectral power shifts to smaller k, plateauing near $k_x = 2 \text{ m}^{-1}$, corresponding to 3 m wavelengths.

The gradient scale length ($L = n_0/\nabla n_0$) perpendicular to the initial trail distribution ranges from 2 to 7 meters over the steepest part of the gradient. The wavenumber of 7 m modes is indicated as a dashed circle in Figure 3. Once the turbulence is well developed, the majority of the spectral power lies in or around this circle. This coincides with the theory of the gradient drift instability, which predicts that the dominant wavelength is about the gradient scale length (Huba & Lee, 1983). Note that as the trail diffuses the gradient length scale increases.

Modes with $k_y = k_z = 0$ are representative of some of the strongest modes in the system, corresponding to waves travel along the trail (in the $\vec{x}$ direction). Figures 4 and 5a show k_x–ω spectra for meteors with and without incident neutral winds. These spectra are generated from the ion distribution after the turbulence is well developed. The spectra show acoustic-like modes with roughly $\omega \propto k$ In the simulation with no neutral wind, the spectrum shows modes moving in both the positive and negative $\vec{x}$ directions, while waves in the simulation with a neutral wind show modes traveling only in the positive $\vec{x}$ direction. Their power exceeds the no-wind amplitude by more than 10 dB, making the waves in the other direction invisible. This agrees with our qualitative analysis of the wave behavior. These spectra also show which modes have the most power along the trail. Visually, the dominant mode is 3 meter waves. The spectra show a broad distribution of power between k=2 and k=6 m^{-1} (1 to 3 meter waves), peaking around $k = 3 \text{ m}^{-1}$. Power significantly decreases for modes with $k > 10 \text{ m}^{-1}$.

Figures 4 and 5a also indicate the ion thermal speed (c_s) for both simulations, and the ion drift velocity (v_d) corresponding to the background electric and magnetic fields for the simulation with a neutral wind. The peak spectral power appears to obey the dispersion relation $\omega = k_x v_d$ in the presence of a neutral wind. In both cases, peak power appears to be bounded by kc_s.

Figure 5b shows the spectrum for a run 15 km higher in altitude than that in Figure 5a, but is otherwise identical. The peak power in the spectrum shifts slightly from $k = 1$–3 m^{-1} to $k = 3$–5 m^{-1} with the change in altitude. The changes in the spectra at higher altitude are due to multiple physical processes. As altitude increases, the

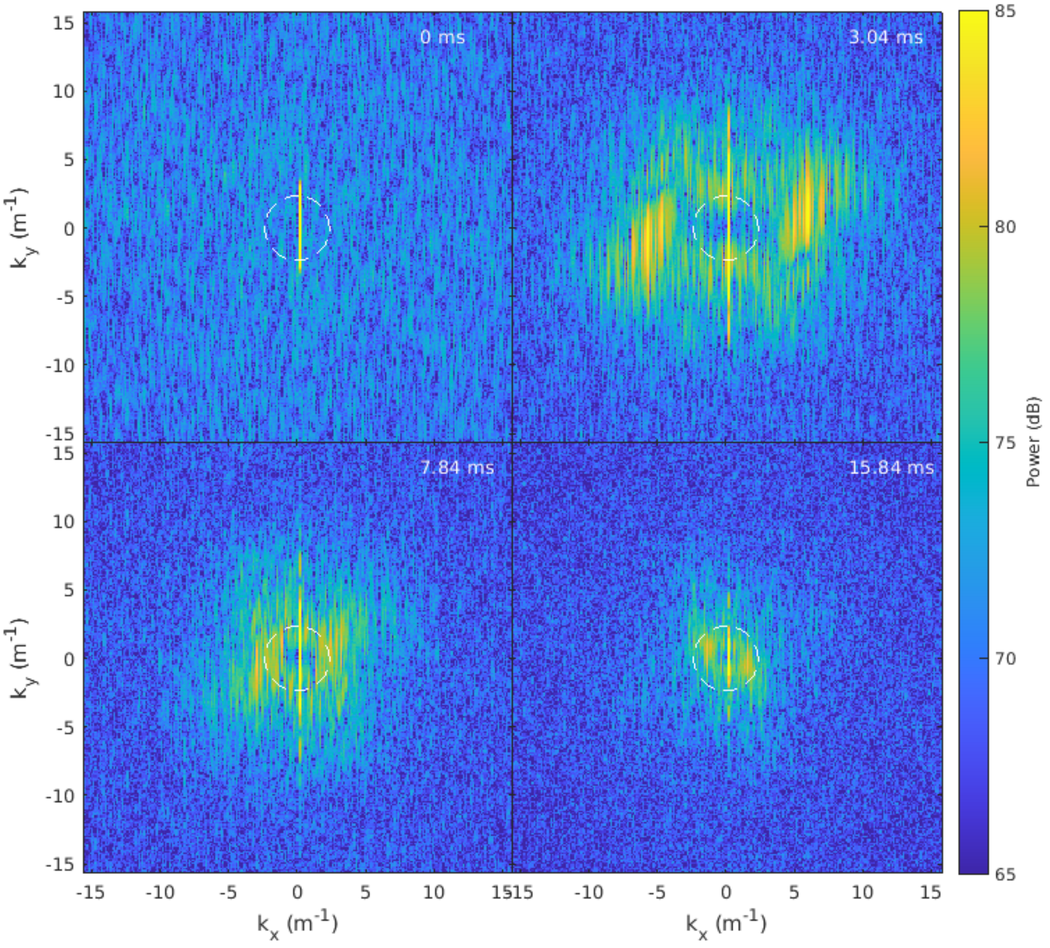

Figure 3. Power spectra, $P(k_x, k_y, k_z = 0)$, over time for a simulation with a 100 m/s neutral wind. A narrow peak at $k_x = 0$ corresponds to the overall structure of the trail. Power develops at large k and shifts to smaller k over the course of the simulation. The wavenumber of the maximum gradient length scale at the beginning of the simulation (7 m) is indicated by the dashed white circle.

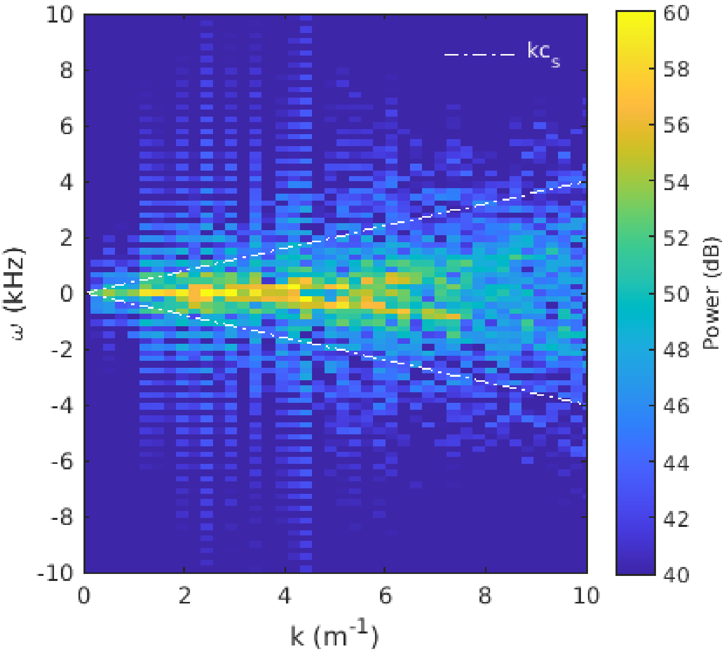

Figure 4. Spectrum of modes with $k_y = k_z = 0$ for a simulation without an incident neutral wind at 100 km. The dashed lines correspond to the ion thermal speed.

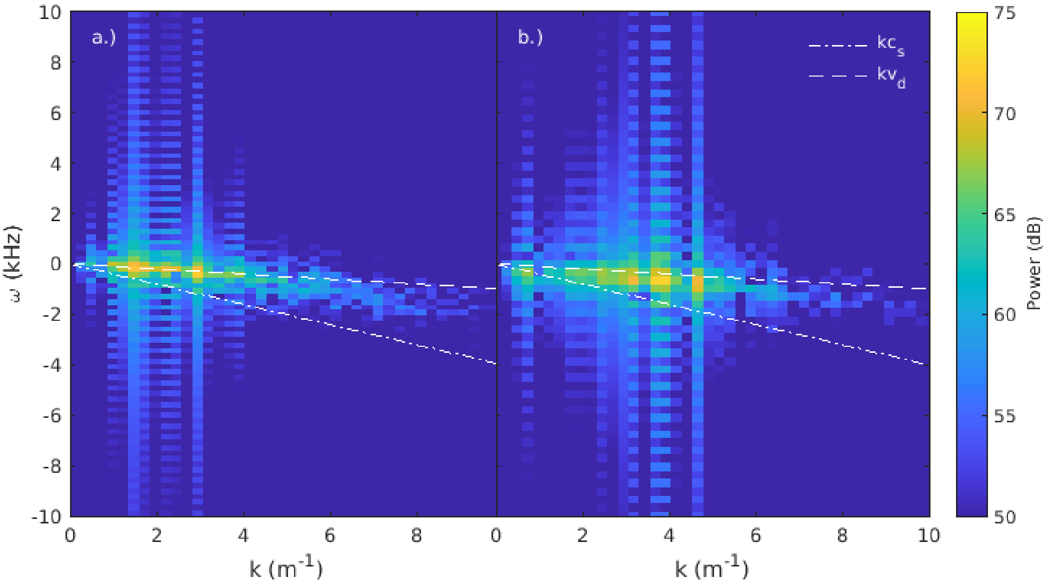

Figure 5. Spectra of modes with $k_y = k_z = 0$ for a simulation with an incident neutral wind at a.) 100 km and b.) 115 km. The dashed and dotted lines correspond to the ion drift velocity due to the background electric and magnetic fields and the ion thermal speed.

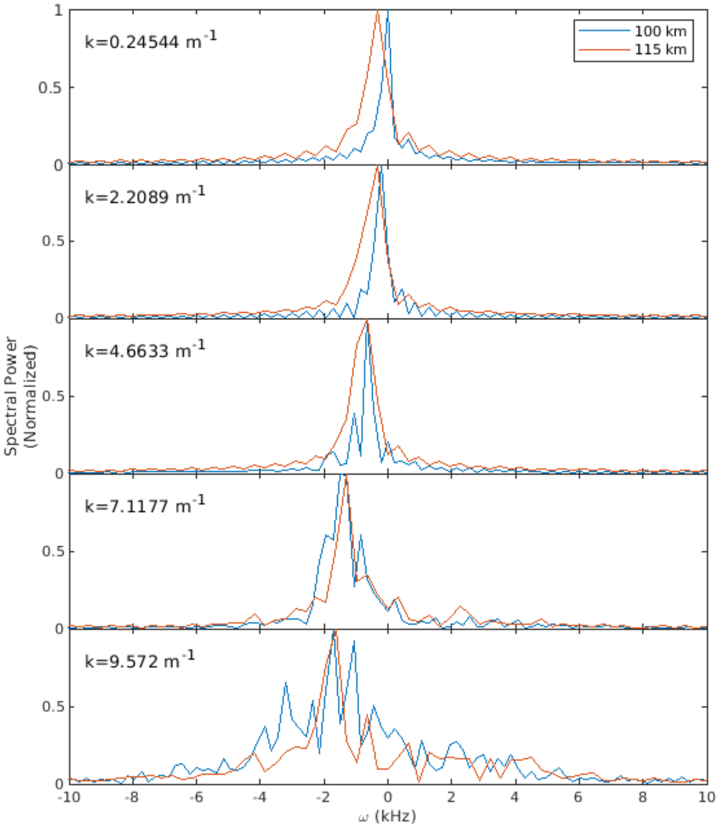

Figure 6. Normalized spectra for two simulations with a 100 m/s neutral wind, at 100 (blue) and 115 km (red). Spectra are perpendicular to $\vec{B}$ at various wavelengths.

background neutral density decreases exponentially. This increases the ion mean free path, which allows the ions of the trail to diffuse faster at higher altitudes and prevents shorter wavelength modes from forming. However, cross-field electron mobility decreases with altitude as the magnetized electrons are tied to field lines. The electrons thus cannot easily follow the diffusing ions, leading to separation of charges and the development of an ambipolar electric field that drives the formation of waves. The developing turbulence is then the mechanism for transporting electrons across $\vec{B}$.

Spectral widths can also be derived from these spectra. Figure 6 shows spectra at single wavenumbers along the trail for simulations with and without a neutral wind at 100 and 115 km. In both cases, the spectra broaden and skew at higher wavenumbers. At smaller wavenumbers (0.2-4.6 m^{-1}) the spectra at higher altitude are broader, and vice versa at larger wavenumbers (7.1-9.6 m^{-1}).

3.3.2 Spectral power off perpendicular to $\vec{B}$

In the simulations, waves propagate primarily along the trail, perpendicular to $\vec{B}$. The following analysis selects individual wavenumbers and investigates spectral power as a function of angle off of $\perp \vec{B}$ (aspect angle). 3 meter modes are analyzed here, corresponding with the observing frequency of the Jicamarca radar. The power at small angles off $\vec{B}$ are of particular interest, as one might expect power to fall off quickly with aspect angle.

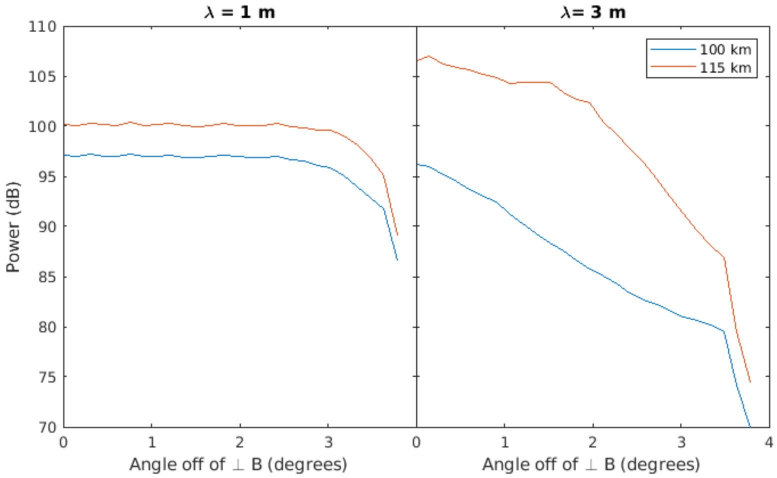

Figure 7. Spectral power in $\lambda = 1, 3$ m modes ($k \approx 6, 2$ m^{-1}) as a function of angle off perpendicular to $\vec{\mathbf{B}}_\mathbf{0}$ for simulations with a neutral wind. Angles have been rescaled to adjust for artificially reduced electron mobility along $\vec{B}$.

To study spectral power as a function of angle, the Fourier transform of ion density is interpolated to a grid as a function of $\vec{k}$ and aspect angle, then average over the frequency dimension. The aspect angles are rescaled by a factor corresponding to the inflated electron mass, to account for increased mobility along $\vec{B}$. Since the perpendicular electron mobility is inversely dependent on m_e ($g_{e\perp}^{Ped} \approx \nu_{en} e/(m_e \Omega_e^2)$, $g_{e\perp}^{H} = e/(m_e \Omega_e)$), PIC electrons have artificially reduced mobility. The angles reported here are rescaled to account for this (see Dimant and Oppenheim (2006)). The selection is restricted to later times in the simulation, once waves have developed fully. All simulation variants produce qualitatively similar results. Figure 7 shows the results for simulations with and without neutral winds at 100 and 115 km. Most power is along the trail, perpendicular to $\vec{B}$. The power in any given wavenumber falls off as a function of aspect angle, as electron mobility along $\vec{B}$ shorts out waves, until the signal is indistinguishable from the noise level in the simulation. However, the presence of a neutral wind significantly affects the relationship with aspect angle. Without a neutral wind, waves develop only at small amplitudes and without much power, even strictly perpendicular to $\vec{B}$. Therefore, spectral power is more distributed as a function of aspect angle.

In general, total spectral power is greater at 115 km than 100 km. At $\lambda = 3$ m, power falls off slightly faster at 115 km ($\approx$ 6.9 dB/degree) than at 100 km ($\approx$ 5.7 dB/degree). At $\lambda = 1$ m the behaviour is qualitatively different. Spectral power is relatively constant for several degrees, then falls off sharply. This is an unexpected result, as radar have previously observed power in 1 m waves dropping off as a function of aspect angle (see 4), and the $k - \omega$ spectra in Figure 5 show that there is some power at 1 m, though less than at 3 m.

4 Discussion & Conclusions

In this paper, a parallel PIC technique is used to model 3D meteor trails under a variety of conditions. Our simulations provide two observable quantities for radars: power as a function of aspect angle and spectral width. While the literature contains little data about the former, as most radar have a fixed angle with respect to $\vec{B}$, a few theoretical and observational studies have been made. Close et al. (2008), using the ALTAIR radar, observed that radar signal strength falls of 3 to 4 dB per degree off of perpendicular to

$\vec{\mathbf{B}}_\mathbf{0}$ at 160 MHz (1.87 meters) for non-specular trails over a range of 6° off perpendicular to $\vec{\mathbf{B}}_\mathbf{0}$. However, Close et al. (2008) used data from just six trails in this analysis, spread over more than 20 degrees of aspect angle and 35 km altitude. While the overall trend is, as reported, a power loss of 3-4 dB per degree, there is enough variation between the data points that the trend may be close to constant at some ranges. Zhou et al. (2004) used numerical simulations to investigate the aspect sensitivity of meteoric field-aligned irregularities, and found that power dropped about 10 dB every 6°, or over 1.5 dB per degree. Our simulations agree more closely with the results from Close et al. (2008), but do not necessarily contradict the results in Zhou et al. (2004). More data from observations and simulations must be collected to draw further conclusions. The simulations are also limited to very small meteors and larger, more realistic ones may develop narrower spectra.

Haldoupis and Schlegel (1993) noted that meteor echoes can have both narrow and broad Doppler spectrum widths, and that the spectral width of an individual trail varies over time. Hall et al. (1997) report spectral widths of several thousand meteor trails observed with the Saskatoon SuperDARN radar. They find that meteor trails have extremely narrow spectral widths, on the order of a few to tens of meters per second. These findings are corroborated in Milan et al. (2001) and Arnold et al. (2001). Arnold et al. (2001) found that spectra broadened with increasing altitude (on the order of 1 m/s per kilometer), and attributed this result to the loss of weak signals at lower altitudes. They also noted an inverse relationship between returned power and spectral width for the same reason. To summarize, they observed high-power, narrow spectra at low altitudes, and weaker, broader spectra at higher altitudes. Bourdillon et al. (2005) observed spectra that are broad at onset, then narrow as the signal decays. However, Chapin and Kudeki (1994) shows meteor spectra that broaden over time. In general, the literature reports much narrower spectra than these simulations produce, by at least an order of magnitude. This discrepancy may simply be due to simulation noise, and might be addressed by performing many simulations and averaging the resulting spectra.

This analysis leaves much work left to be done. As computing facilities improve, more extensive simulations can be performed, increasing box size and resolution as well as approaching the true parameters of the physical system. Even with existing computational abilities, this work leaves a broad parameter space unexplored. The effects of altitude and neutral wind speed on spectra can be investigated with more resolution, as well as additional parameters not included in this work such as peak trail density, temperature, and neutral wind sheer. Improving the physicality of the simulations and investigating the effect of varying additional parameters will improve our theoretical understanding of the system and provide better comparisons to observational data.

Simulations of short trail ”segments” show that the trail tends to drift with the neutral wind, as one would expect. Neutral winds also stimulate the growth of turbulence; without a neutral wind, only small amplitude waves develop. Spectral analysis shows that waves develop first at short wavelengths, then grow to longer wavelengths. Most wave power develops between $k = 2$ and $k = 6$ m^{-1}. This indicates that the instability is gradient-driven. If a neutral wind is present, the peak spectral power tends to follow the dispersion relation $\omega = kv_d$, where v_d is the ion drift speed due to external fields. Spectral power is also concentrated perpendicular to $\vec{B}$, and falls off as a function of aspect angle. Finally, spectra broaden and skew as a function of wavenumber. These results improve our theoretical understanding of the evolution of meteor trails, and can be used to compare to radar observations.

Acknowledgments

This work was supported by NSF grant ATM-1007789 and NASA award NNx11AO96G. Computation was performed using the TACC computational facility at University of Texas at Austin, supported by NSF grant AcI-1053575, and with the Shared Computing Clus-

ter at Boston University. The source code and input files used to produce the simulations in this work are archived at http://doi.org/10.5281/zenodo.4252708. Simulation outputs are archived on the TACC Stampede 2 system; TACC account holders who wish to access this data directly should contact the corresponding author.

References

Arnold, N., Robinson, T., Lester, M., Byrne, P., & Chapman, P. (2001, 04). Super dual auroral radar network observations of fluctuations in the spectral distribution of near range meteor echoes in the upper mesosphere and lower thermosphere. *Annales Geophysicae*, *19*. doi: 10.5194/angeo-19-425-2001

Birdsall, C. K., & Langdon, A. B. (1985). *Plasma physics via computer simulation.* McGraw-Hill, New York.

Bourdillon, A., Haldoupis, C., Hanuise, C., Roux, Y. L., & Menard, J. (2005). Long duration meteor echoes characterized by doppler spectrum bifurcation. *Geophys. Res. Lett.*, *32*. doi: 10.1029/2004GL021685

Chapin, E., & Kudeki, E. (1994). Plasma wave excitation on meteor trails in the equatorial electrojet. *Geophys. Res. Lett.*, *21*. doi: 10.1029/94GL01705

Chau, J. L., & Woodman, R. F. (2004). Observations of meteor-head echoes using the jicamarca 50mhz radar in interferometer mode. *Atmospheric Chemistry and Physics*, *4*(2), 511–521. doi: 10.5194/acp-4-511-2004

Close, S., Hamlin, T., Oppenheim, M., Cox, L., & Colestock, P. (2008). Dependence of radar signal strength on frequency and aspect angle of nonspecular meteor trails. *Journal of Geophysical Research: Space Physics*, *113*(A6). doi: 10.1029/2007JA012647

Close, S., Oppenheim, M., Durand, D., & Dyrud, L. (2005). A new method for determining meteoroid mass from head echo data. *Journal of Geophysical Research: Space Physics*, *110*(A9). doi: 10.1029/2004JA010950

Dimant, Y. S., & Oppenheim, M. M. (2006). Meteor trail diffusion and fields: 1. simulations. *Journal of Geophysical Research: Space Physics*, *111*(A12). doi: 10.1029/2006JA011797

Dimant, Y. S., Oppenheim, M. M., & Milikh, G. M. (2009). Meteor plasma trails: effects of external electric field. *Annales Geophysicae*, *27*(1), 279–296. doi: 10.5194/angeo-27-279-2009

Dyrud, L., Oppenheim, M., Close, S., & Hunt, S. (2012, 01). Interpretation of non-specular radar meteor trails. *Geophys. Res. Lett*, *29*. doi: 10.1029/2002GL015953

Eshleman, V. R. (1955). Theory of radio reflections from electron-ion clouds. *Transactions of the IRE Professional Group on Antennas and Propagation*, *3*(1), 32-39.

Haldoupis, C., & Schlegel, K. (1993). A 50-mhz radio doppler experiment for midlatitude e region coherent backscatter studies: System description and first results. *Radio Science*, *28*(06), 959-978.

Hall, G. E., MacDougall, J. W., Moorcroft, D. R., St.-Maurice, J.-P., Manson, A. H., & Meek, C. E. (1997). Super dual auroral radar network observations of meteor echoes. *Journal of Geophysical Research: Space Physics*, *102*(A7), 14603-14614. doi: 10.1029/97JA00517

Hocking, W. K., & Thayaparan, T. (1997). Simultaneous and colocated observation of winds and tides by mf and meteor radars over london, canada (43° n, 81° w), during 19941996. *Radio Science*, *32*(2), 833-865. doi: 10.1029/96RS03467

Huba, J. D., & Lee, L. C. (1983). Short wavelength stabilization of the gradient drift instability due to velocity shear. *Geophysical Research Letters*, *10*(4), 357-360. doi: 10.1029/GL010i004p00357

Kelley, M., Alcala, C., & Cho, J. (1998). Detection of a meteor contrail and meteoric dust in the earth's upper mesosphere. *Journal of Atmospheric and*

Solar-Terrestrial Physics, *60*(3), 359 - 369. doi: https://doi.org/10.1016/S1364-6826(97)00113-2

Lee, C., Kim, J.-H., Jee, G., Lee, W., Song, I.-S., & Kim, Y. H. (2016). New method of estimating temperatures near the mesopause region using meteor radar observations. *Geophysical Research Letters*, *43*(20), 10,580-10,585. doi: 10.1002/2016GL071082

Liu, L., Liu, H., Le, H., Chen, Y., Sun, Y.-Y., Ning, B., . . . Xiong, J. (2017). Mesospheric temperatures estimated from the meteor radar observations at mohe, china. *Journal of Geophysical Research: Space Physics*, *122*(2), 2249-2259. doi: 10.1002/2016JA023776

Michell, R., Janches, D., Samara, M., Hormaechea, J., Brunini, C., & Bibbo, I. (2015). Simultaneous optical and radar observations of meteor head-echoes utilizing saamer. *Planetary and Space Science*, *118*, 95 - 101. (SI:ACM Interrelated) doi: https://doi.org/10.1016/j.pss.2015.04.018

Milan, S., Lester, M., Sato, N., & Takizawa, H. (2001, 02). On the altitude dependence of the spectral characteristics of decametre-wavelength e region backscatter and the relationship with optical auroral forms. *Annales Geophysicae*, *19*. doi: 10.5194/angeo-19-205-2001

Oppenheim, M., & Dimant, Y. (2004). Ion thermal effects on e-region instabilities: 2d kinetic simulations. *Journal of Atmospheric and Solar-Terrestrial Physics*, *66*(17), 1655 - 1668. (40 Years of Equatorial Aeronomy Sparked by the Jicamarca Radio Observatory) doi: https://doi.org/10.1016/j.jastp.2004.07.007

Oppenheim, M., & Dimant, Y. (2006). Meteor induced ridge and trough formation and the structuring of the nighttime e-region ionosphere. *Geophysical Research Letters*, *33*(24). doi: 10.1029/2006GL028267

Oppenheim, M., & Dimant, Y. (2013, 03). Kinetic simulations of 3-d farley-buneman turbulence and anomalous electron heating. *Journal of Geophysical Research (Space Physics)*, *118*, 1306-1318. doi: 10.1002/jgra.50196

Oppenheim, M., & Dimant, Y. S. (2015). First 3-d simulations of meteor plasma dynamics and turbulence. *Geophysical Research Letters*, *42*(3), 681-687. doi: 10.1002/2014GL062411

Oppenheim, M., Sugar, G., Bass, E., Dimant, Y. S., & Chau, J. (2008). Day to night variation in meteor trail measurements: Evidence for a new theory of plasma trail evolution. *Geophysical Research Letters*, *35*(3). doi: 10.1029/2007GL032347

Sugar, G., Oppenheim, M. M., Dimant, Y. S., & Close, S. (2018). Formation of plasma around a small meteoroid: Simulation and theory. *Journal of Geophysical Research: Space Physics*, *123*(5), 4080-4093. doi: 10.1002/2018JA025265

Sugar, G. R. (1964). Radio propagation by reflection from meteor trails. *Proceedings of the IEEE*, *52*(2), 116-136.

Wen, Y., Jin-Song, C., Chun-Bo, M., Na, L., & Zhen-Wei, Z. (2014). Observation of upper atmospheric temperature by kunming all-sky meteor radar. *Chinese Journal Of Geophysics*, *57*(8), 2423. doi: 10.6038/cjg20140804

Zhou, Q. H., Morton, Y. T., Mathews, J. D., & Janches, D. (2004). Aspect sensitivity of vhf echoes from field aligned irregularities in meteor trails and thin ionization layers. *Atmospheric Chemistry and Physics*, *4*(3), 685–692. doi: 10.5194/acp-4-685-2004

Figure 1.

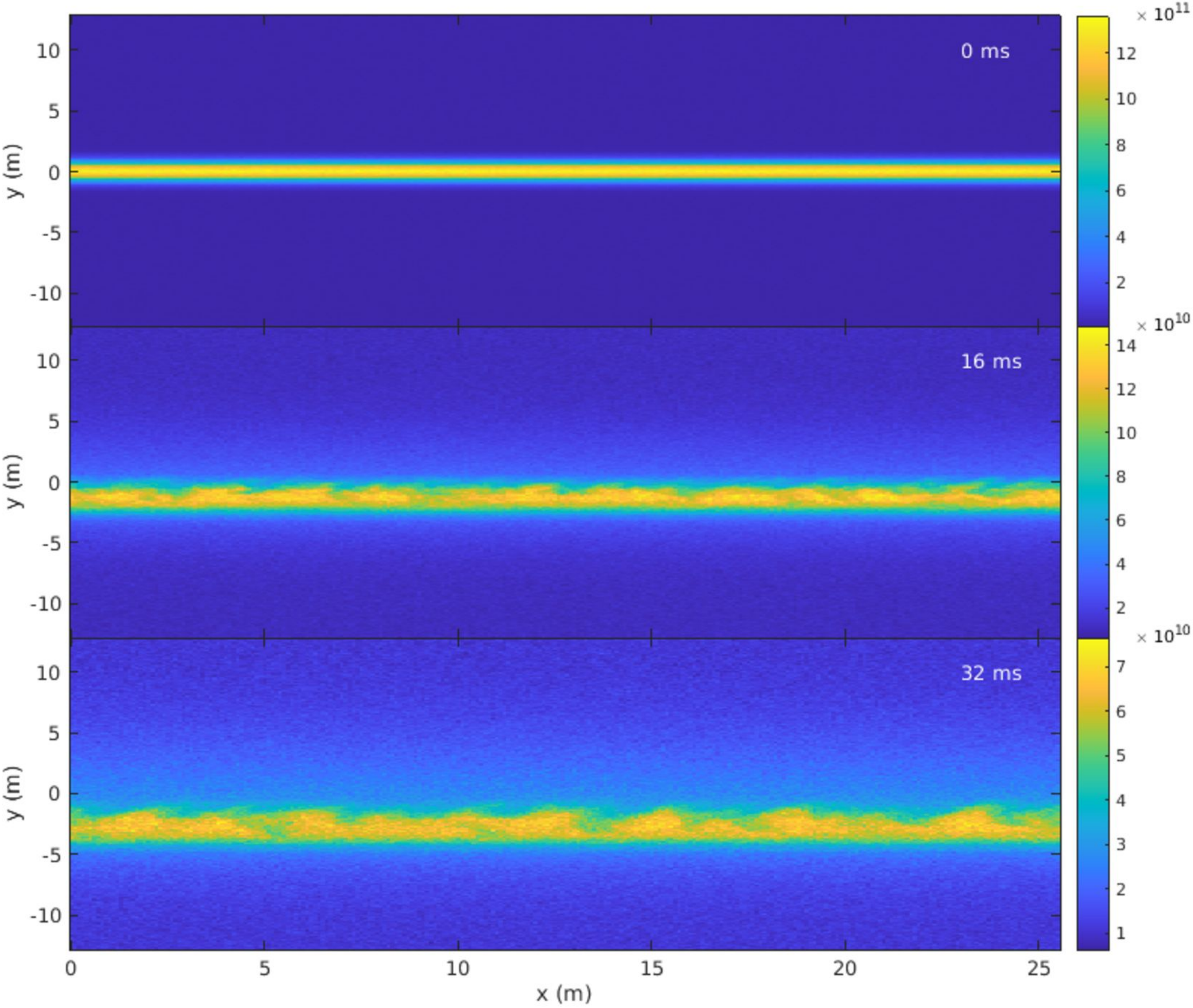
0 ms
16 ms
32 ms
y (m)
x (m)
× 10^11
× 10^10
× 10^10
10
5
0
-5
-10
0
5
10
15
20
25
12
10
8
6
4
2
14
12
10
8
6
4
2
7
6
5
4
3
2
1

Figure 2.

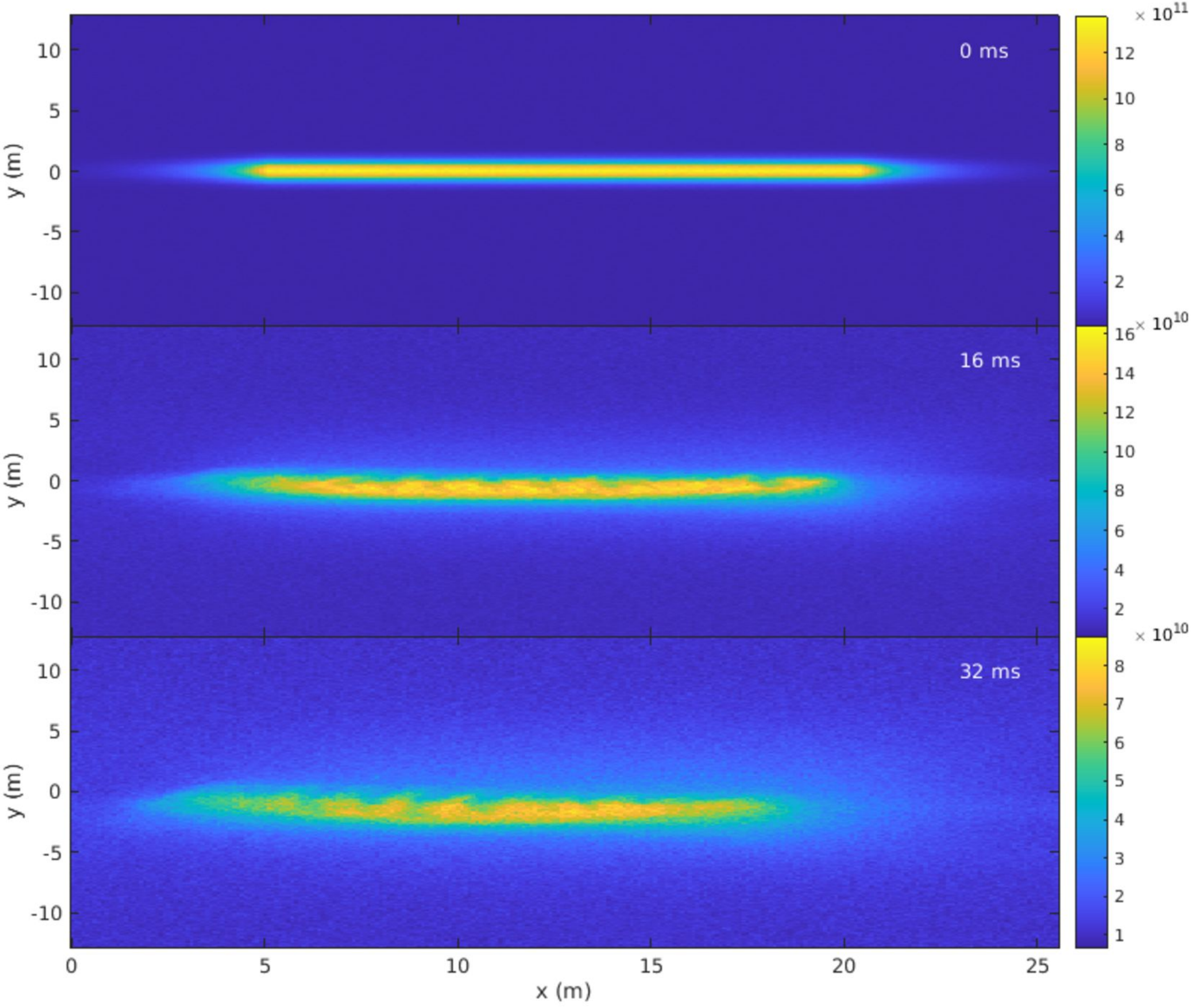
0 ms
16 ms
32 ms
y (m)
x (m)
10
5
0
-5
-10
0
5
10
15
20
25
× 10^11
12
10
8
6
4
2
× 10^10
16
14
12
10
8
6
4
2
× 10^10
8
7
6
5
4
3
2
1

Figure 3.

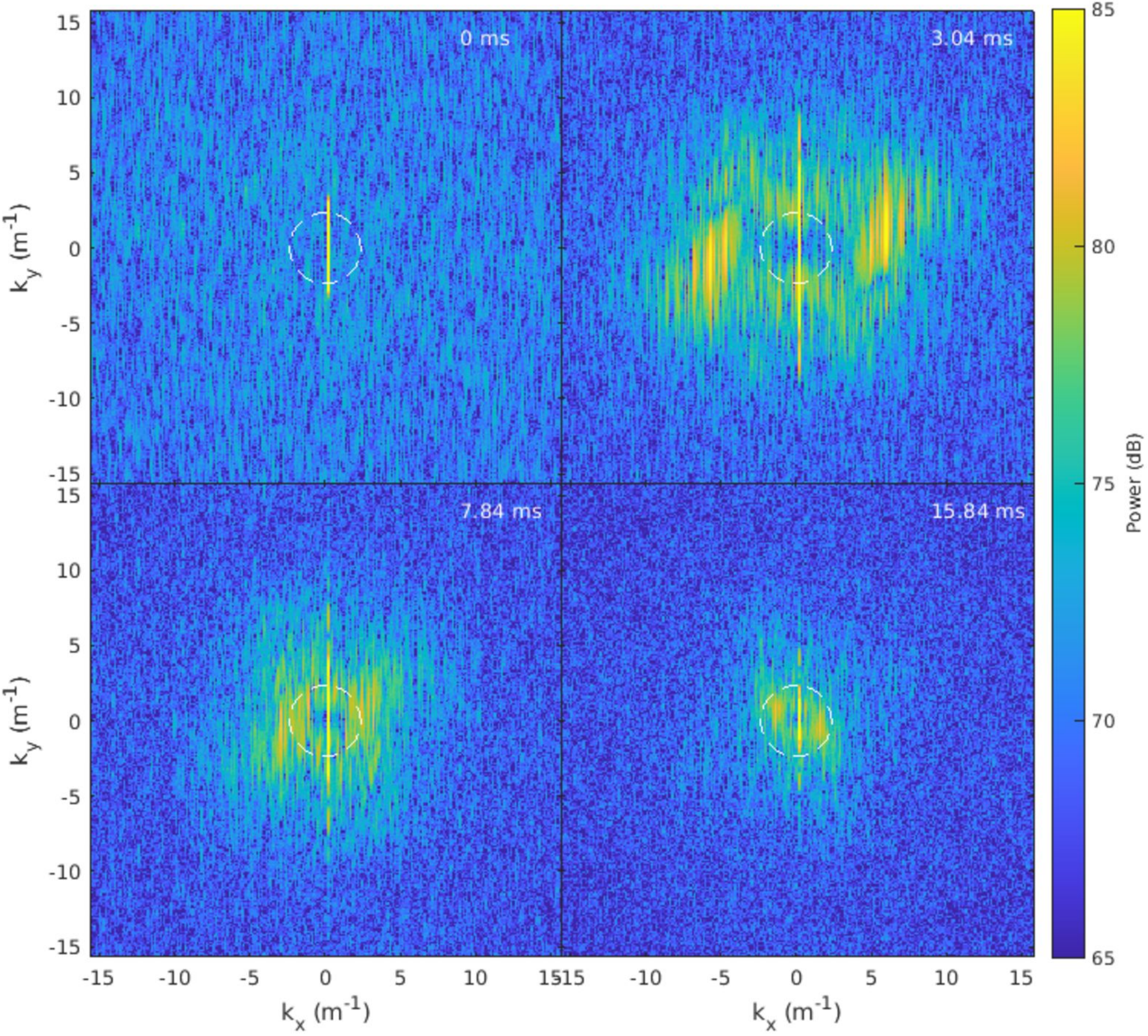
0 ms
3.04 ms
7.84 ms
15.84 ms
k_y (m^{-1})
k_x (m^{-1})
15
10
5
0
-5
-10
-15
Power (dB)
85
80
75
70
65

Figure 4.

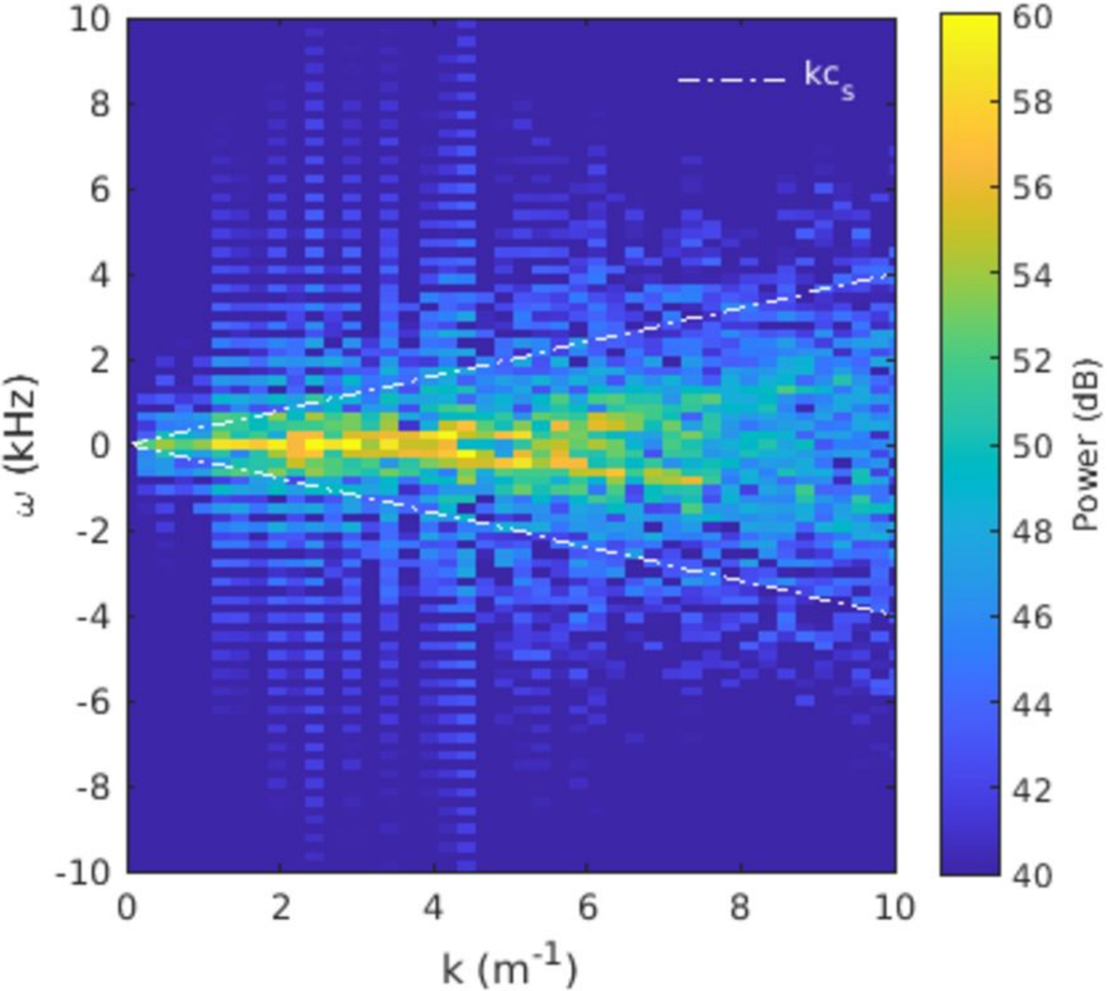
kc_s
ω (kHz)
k (m^-1)
Power (dB)
10
8
6
4
2
0
-2
-4
-6
-8
-10
0
2
4
6
8
10
60
58
56
54
52
50
48
46
44
42
40

Figure 5.

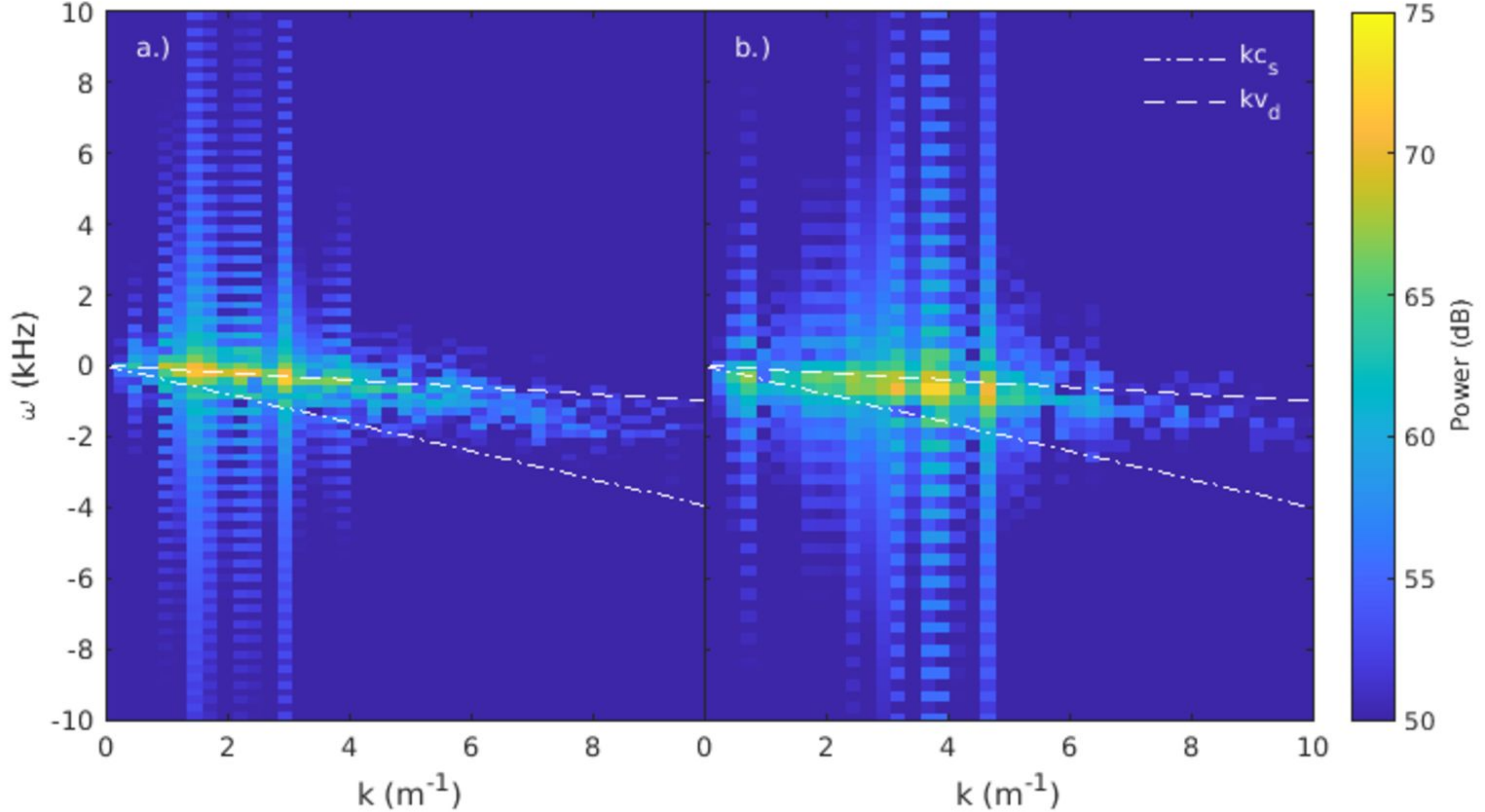
a.)
b.)
kc_s
kv_d
ω (kHz)
k (m^{-1})
k (m^{-1})
Power (dB)
10
8
6
4
2
0
-2
-4
-6
-8
-10
0
2
4
6
8
10
75
70
65
60
55
50

Figure 6.

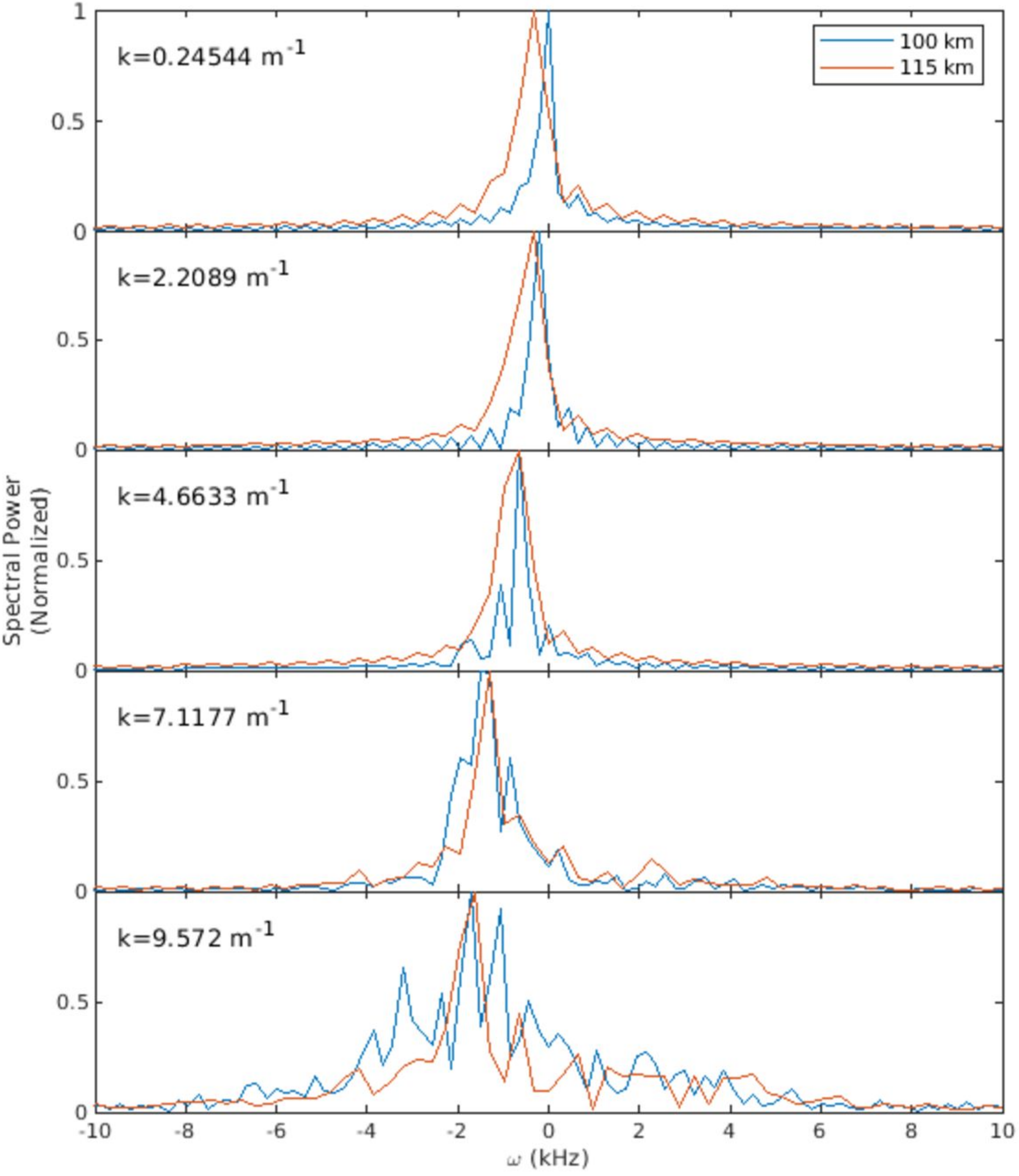
100 km
115 km
k=0.24544 m^{-1}
k=2.2089 m^{-1}
k=4.6633 m^{-1}
k=7.1177 m^{-1}
k=9.572 m^{-1}
Spectral Power
(Normalized)
1
0.5
0
ω (kHz)
-10
-8
-6
-4
-2
0
2
4
6
8
10

Figure 7.

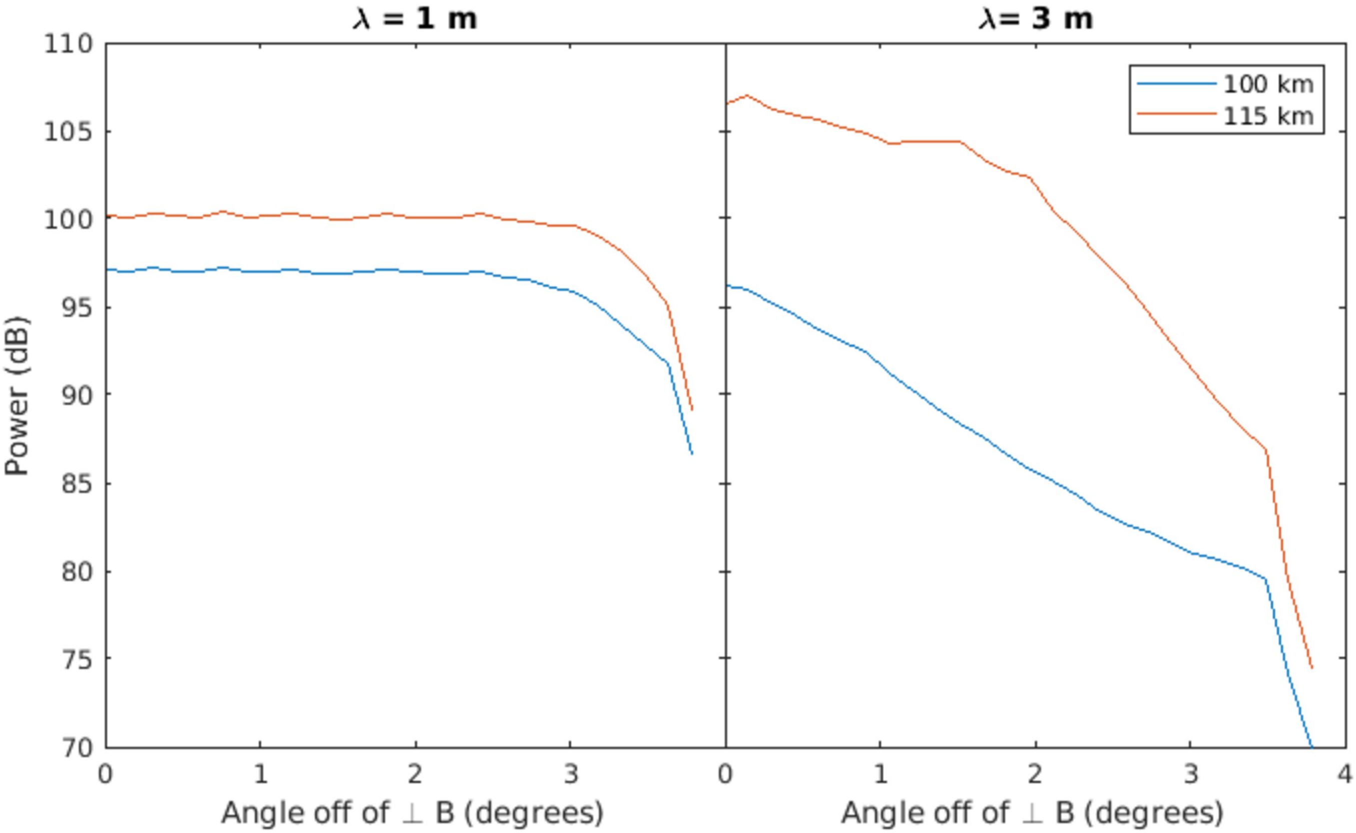
λ = 1 m
λ= 3 m
100 km
115 km
Power (dB)
110
105
100
95
90
85
80
75
70
0
1
2
3
0
1
2
3
4
Angle off of ⊥ B (degrees)
Angle off of ⊥ B (degrees)